THE JOURNAL OF PHYSICAL CHEMISTRY C
A JOURNAL OF THE AMERICAN CHEMICAL SOCIETY

pubs.acs.org/JPCC

Article

# Oxygen Functionalization Reshapes the Electrochemical Interface of Single-Layer Graphene via Defect Evolution and Ion Structuring

Xiaolan Wang,[▽] Wei Guo,[▽] Kun Ni,[▽] Jun Ma, Jiawei Xue,* Zhaohui Wang, Jun Bao, and Yanwu Zhu*

Cite This: J. Phys. Chem. C 2025, 129, 14993−15002

Read Online

ACCESS | Metrics & More | Article Recommendations | Supporting Information

**ABSTRACT:** Chemical modification, though vital for tailoring graphene-based supercapacitor electrodes, leaves the molecular-scale origins of its impact on the electrochemical stability and interfacial charge storage kinetics unresolved. Here, we uncover how oxygen functionalization modulates the structural integrity and ion dynamics of single-layer graphene (SLG) in an ionic liquid electrolyte using ex situ Raman spectroscopy, in situ sum-frequency generation spectroscopy, and electrochemical impedance spectroscopy, coupled with numerical modeling. We find that oxygen functionalization is electrochemically unstable, leading to defect formation during cyclic voltammetry. An interfacial ion organization is observed: at negative potential, cations adopt a near-planar orientation; at positive potential, the anion adsorption is enhanced. This behavior contrasts with pristine SLG, where cations exhibit a potential-dependent twist. These interfacial modifications lead to ionic relaxation yet increase the overall capacitance, highlighting a fundamental trade-off between charge storage capacity and long-term stability in chemically modified graphene electrodes.

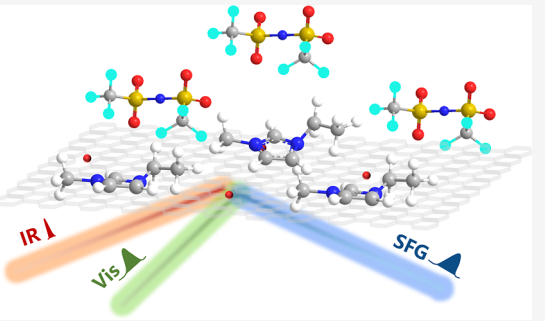


## INTRODUCTION

Since the last century, commercial supercapacitors have predominantly used activated carbons as the electrode material due to the plenty of pores in activated carbons typically prepared with cost-effective activation technique.[1] Compared to the reported electrical conductivity of about 39 S $m^{-1}$ for an activated carbon,[2] graphene-based materials offer a significantly higher conductivity of up to $1 \times 10^4$ S $m^{-1}$[3] while maintaining a high specific surface area (SSA) of 2630 $m^2$ $g^{-1}$ for graphene[4] or even a higher value of 3100 $m^2$ $g^{-1}$ for porous carbons derived from graphene.[5] Based on a graphene-derived electrode made by immersing graphene platelets in 0.065 M 1-ethyl-3-methylimidazolium tetrafluoroborate ($[EMIM]^+[BF_4]^-$) ionic liquid and subsequent vacuum drying, a capacitance of 209.0 F $g^{-1}$ at 0.1 A $g^{-1}$ and a volumetric energy density of 59.9 W h $L^{-1}$ have been achieved.[6] In another study, a film (SSA ∼ 612 $m^2$ $g^{-1}$) made by hydriodic acid (HI) reduced mixture of graphene (75 wt %) and graphene oxide (25 wt %) demonstrated a capacitance of 231 F $g^{-1}$ at 1 A $g^{-1}$ and a volumetric energy density of 88.1 W h $L^{-1}$ in neat 1-ethyl-3-methylimidazolium tetrafluoroborate ($[EMIM]^+[TFSI]^-$) electrolyte.[7]

Chemical modification in graphene has been extensively employed to enhance the energy storage performance of graphene-based supercapacitors through increasing the adsorption site of electrode materials,[8] improving the wettability of the electrode to electrolyte,[9] or introducing pseudocapacitance by increasing the redox reactions.[10] Single- or multielement doping (N/S/B) tailors functional properties in graphene electrodes, in which the nitrogen doping in reduced graphene oxide (rGO) boosts aqueous-phase redox activity,[11] evidenced by Faradaic humps in cyclic voltammetry.[12] Theoretical simulations confirm that N-doping injects electrons into $\pi$-orbitals of graphene and modulates Fermi levels, enhancing the quantum capacitance.[13] Similarly, S-doping triggers pseudocapacitance via thiocarboxylic ester-to-sulfone conversion,[9] while oxygen functional groups such as COOH/C−OH groups contribute 21.92 F (g at. %)$^{-1}$ pseudocapacitance in 1 M $H_2SO_4$, while C═O groups provide 28.22 F (g at. %)$^{-1}$.[14] Notably, excessive carbonyl groups in 6 M KOH increase Warburg impedance, compromising ionic mobility.[15] Despite the promising improvement in performance, the mechanistic understanding of how these chemical modifications enhance performance has been insufficiently explored, limiting the optimization of these strategies.

Advanced in situ characterization techniques, including Fourier transform infrared spectroscopy,[16] Raman spectroscopy,[17] atomic force microscopy (AFM),[18] and synchrotron X-ray scattering,[19] provide insights into the dynamics of the interfacial reconstruction on graphene electrodes. Among

Received: April 5, 2025
Revised: July 19, 2025
Accepted: July 31, 2025
Published: August 8, 2025

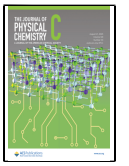






https://doi.org/10.1021/acs.jpcc.5c02290
J. Phys. Chem. C 2025, 129, 14993−15002

these, forbidden in bulk phases with inversion symmetry, sum-frequency generation (SFG) spectroscopy uniquely probes interfacial species with molecular-level sensitivity, directly revealing their orientation and interaction at the electrode/electrolyte interface.[20,21] SFG analysis of the single-layer graphene (SLG) interface in the absence of an applied electric field reveals concurrent cation/anion presence, with anions tilted and cation butyl chains primarily oriented parallel to the graphene surface plane, driven by substrate-induced polarization, $\pi-\pi$ interactions, and van der Waals forces, contradicting the conventional cation-centric hydrophobic adsorption model on nonpolar surfaces in 1-butyl-3-methylimidazolium methane sulfate electrolyte.[22,23] In situ SFG spectroscopy reveals a potential-dependent interfacial reorganization of ionic liquid on triple-layer graphene: butyl-3-methylimidazolium dicyanamide ($[BMIM]^+[DCA]^-$) exhibits enhanced $[DCA]^-$ signal intensity at positive potentials (indicating anion ordering or density increase) while maintaining the stable interfacial orientation under negative polarization.[24] However, these investigations predominantly focus on chemically inert graphene surfaces, leaving a critical gap: how deliberate surface functionalization modulates the interfacial architecture and ionic kinetics. As SLG can avoid the influence of confinement, the investigation using SLG as a model to observe the effect of the modification could be more straightforward.

In this work, SLG treated with oxygen plasma (resulting in sample called O-SLG) has been used as the electrode in $[EMIM]^+[TFSI]^-$ electrolyte and subjected to Raman spectroscopy, SFG, and electrochemical impedance spectroscopy (EIS) studies, validated through numerical simulations. It is found that oxygen-containing functional groups on the SLG can enhance the capacity of electrode materials by altering the configuration of ion adsorption. At the same time, the presence of these functional groups compromises the stability of the electrode material and slows ion kinetics, presenting a trade-off between capacity enhancement and cycling performance.

## EXPERIMENTAL SECTION

**Preparation of Samples and Chemicals.** The SLG grown on copper foil purchased from Ningbo Soft Carbon Electronic Technology Co., Ltd. was transferred to the target substrate by a poly(methyl methacrylate)-assisted method.[25] For oxygen functionalization, plasma treatment was performed using a Pluto-30 plasma cleaning system (Shanghai Peiyuan Instrument Equipment Co., Ltd.) under controlled conditions: a base chamber pressure of 100 mTorr and an oxygen plasma generated at a 10 W radio frequency power with a sustained $O_2$ gas flow rate of 25 sccm. The samples were subjected to an optimized plasma exposure protocol for 5 s to achieve controlled oxygen functionalization. Cyclic voltammetry (CV) measurement was performed using PARSTAT4000 (AMETEK Scientific Instruments) in a three-electrode configuration: working electrode (SLG or O-SLG on quartz, geometric area 0.785 $cm^2$), reference electrode (Pt wire), and counter electrode (Pt wire). The potential was scanned between −0.8 V and +0.9 V vs Pt at 20 mV $s^{-1}$. The electrolyte $[EMIM]^+[TFSI]^-$ (>99.9% purity) was procured from Lanzhou Greenchem ILs.

**Characterizations.** *Angle-Resolved XPS (ARXPS).* Surface-sensitive chemical analysis was conducted at shallow takeoff angles (defined as the angle between the detector and sample normal) of 10° and 60° using a Thermo Scientific K-Alpha system (Thermo Fisher Scientific, Inc.) with monochromatic Al K$\alpha$ radiation (1486.6 eV). $CaF_2$ was used as a substrate.

*Infrared Free Electron Laser Nanospectroscopy (AFM-IRFEL).* AFM-IRFEL was performed at the AFM-IRFEL station of the FELiChEM free electron laser facility in National Synchrotron Radiation Laboratory (Hefei, China), operating with a top-down incident mode. In the measurement, a pulsed, broadly tunable IRFEL was employed as the infrared (IR) source, which offers a maximum power of less than 100 mJ/pulse and a spectral coverage range of 2−200 $\mu$m. AFM worked in contact mode using a gold-coated probe (PR-EX-nIR2, resonant frequency 13 ± 4 kHz, and force constant 0.07−0.4 N/m, Anasys Instruments). The spectra were collected at the resolution of 4 $cm^{-1}$ and referenced to the background spectrum obtained from the measurement of the wavelength-dependent laser power.

*Ellipsometry.* Ellipsometry was conducted using an ME-L-L ellipsometer (Wuhan Eoptics Technology Co., Ltd.). Data were acquired at 65° incident angles with 1 nm spectral resolution in the 300−1000 nm range. Optical constants such as refractive index $n$ and extinction coefficient $k$ were extracted through Eometrics software using a model using $SiO_2$ as the substrate, fitting $\Psi$ and $\Delta$ parameters with the Drude−Lorentz model. Quartz was used as the substrate.

*Energy-Dispersive X-ray Spectroscopy.* Energy-dispersive X-ray spectroscopy (EDS) was performed on an FEI Apreo SEM (Thermo Fisher Scientific, Inc.) equipped with a Bruker XFlash 6130 detector, operating at an accelerating voltage of 5 kV and a probe current of 10 nA. Elemental quantification was conducted with 60 s acquisition time per scan to ensure sufficient counting statistics. Quartz was used as the substrate.

*Raman Spectroscopy.* Raman spectroscopic mapping was carried out using an RM3000 system with 532 nm excitation (5 mW, 50× objective, Renishaw Plc.). Quartz was used as the substrate. A 120 × 120 $\mu m^2$ area square Au frame with 10 $\mu$m wide edge was prepatterned on the substrate prior to SLG transfer, enclosing an uncoated region with an area of 100 × 100 $\mu m^2$. Hyperspectral data sets (20 × 20 $\mu m^2$ area, 1 $\mu$m step size) were acquired in the 1200−3000 $cm^{-1}$ range (2 $cm^{-1}$ spectral resolution). The D to G intensity ratio ($I_D/I_G$) and 2D to G intensity ratio ($I_{2D}/I_G$) were processed via Wire 3.0 software with cosmic ray removal and baseline correction algorithms.

*SFG Spectroscopy.* SFG spectroscopy setup was based on a 35 fs Ti:sapphire laser system (Astrella, Coherent) that provides the fundamental 800 nm laser beam with 6 mJ/pulse at a 1 kHz repetition rate. A small portion of the amplifier output (∼10%) was passed through a narrowband filter (808 nm, 3 nm full width at half-maximum (fwhm), Semrock) and an air-gap Etalon (800 nm, 1 nm fwhm, SLS Optics Ltd.) to generate the narrowband visible (VIS) beam with ∼9 $cm^{-1}$. The rest of the amplifier output was used to generate the tunable broadband IR with a commercial optical parametric amplifier (TOPAS, Light Conversion) and noncollinear difference-frequency generation (Light Conversion). The VIS and tunable broadband IR beams were spatially and temporally overlapped at the sample surface with incident angles of 57° and 63° with respect to the surface normal and with spot diameters of ∼260 and ∼500 $\mu$m, respectively. With spectral and spatial filtering, the SFG signal was detected with a spectrograph (iHR 320, HORIBA Scientific) equipped with a 1200 grooves/mm grating and a charge-coupled device detector (Syncerity, HORIBA Scientific). The in situ SFG


https://doi.org/10.1021/acs.jpcc.5c02290
J. Phys. Chem. C 2025, 129, 14993−15002

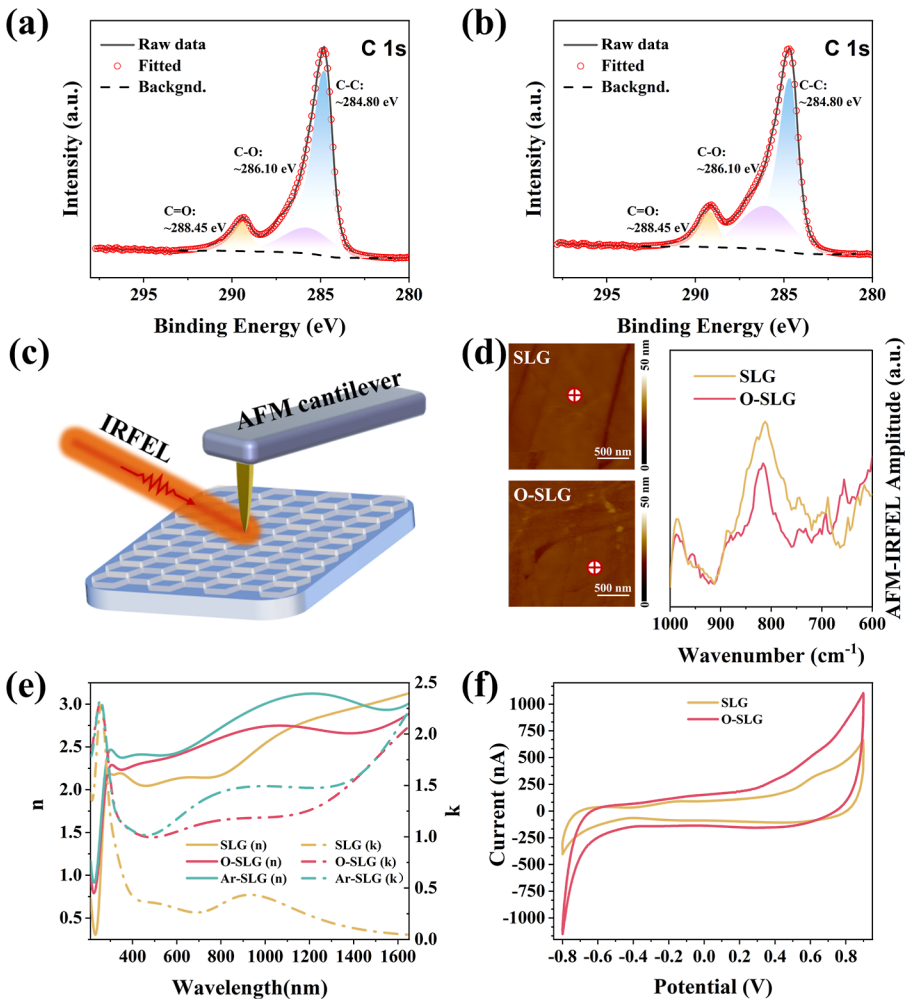


**Figure 1.** ARXPS C 1s spectra of (a) SLG and (b) O-SLG, exhibiting three characteristic components: C−C/C═C at 284.80 eV, C−O at 285.67 eV, and C═O at 288.99 eV at a takeoff angle of 60°. (c) Schematic illustration of AFM-IRFEL. (d) AFM images (left) and the corresponding IRFEL spectra (right) acquired at the white cross-marked positions in the AFM images. (e) *n*, *k* values of SLG, O-SLG, and Ar-SLG. (f) CV curves of SLG and O-SLG in the voltage range of −0.8 V to +0.9 V. The sweep speed is 20 mV $s^{-1}$.

measurement was performed by the total internal reflection geometry (Figure S1), which allows for observing the SLG electrode/electrolyte interface without IR absorption from the bulk electrolyte solution. The SFG spectra were collected in the PPP (P-polarized SFG, P-polarized VIS, and P-polarized IR) polarization combination.

*Simulation.* Molecular dynamics (MD) simulations were conducted using the Forcite module in Materials Studio software with the COMPASSII force field. Systems with charged electrodes of −0.03, −0.06, and +0.06 e/C atoms were simulated. The simulation model is illustrated in Figure S2. Density functional theory (DFT) calculations was performed with Vienna Ab initio Simulation Package.[26] The Perdew−Burke−Ernzerhof[27] exchange−correlation functional with generalized gradient approximation[28] was adopted. The van der Waals interaction was described by the DFT-D3 method[29] with Becke−Johnson damping (BJ-D3).[30] The energy cutoff of the plane-wave basis set was 500 eV. The force tolerance for geometry optimization was −0.02 eV/Å.

*Electrochemical Impedance Spectroscopy.* EIS data were acquired using a PARSTAT4000. Measurement was conducted in a three-electrode configuration (working electrode: SLG/O-SLG on the quartz substrate; reference: Pt wire; counter: Pt wire) in a potential window of −0.8 to 0.9 V vs Pt (0.05 V/step) under potentiostatic control. At each potential, impedance data were collected over 240 frequency decades (100 kHz−0.1 Hz, 40 points/decade) with a 10 mV RMS sinusoidal perturbation. The real and imaginary capacitance components versus frequency were extracted using VersaStudio software.

## RESULTS AND DISCUSSION

The SLG transferred on $CaF_2$ was treated with low-power oxygen plasma to obtain O-SLG. Due to the atomically thin thickness and the low overall elemental content of SLG and O-SLG, the energy-dispersive spectrometry (EDS) performed in a scanning electron microscope (SEM) could not be used to determine the elemental composition in doped samples, as shown in Figure S3. Instead, ARXPS was employed owing to its unparalleled surface sensitivity compared to normal XPS.[31] As shown in Figure 1a,b, the ARXPS analysis of C 1s at a takeoff angle of 60° resolves three chemically distinct components: C−C/C═C bond at 284.80 eV (68.85% area fraction for pristine SLG; 31.69% for O-SLG), C−O bond at 286.10 eV (20.24% → 56.85%), and C═O moieties at 288.45 eV (10.91% → 11.46%). At a takeoff angle of 10°, the near-


https://doi.org/10.1021/acs.jpcc.5c02290
J. Phys. Chem. C 2025, 129, 14993−15002

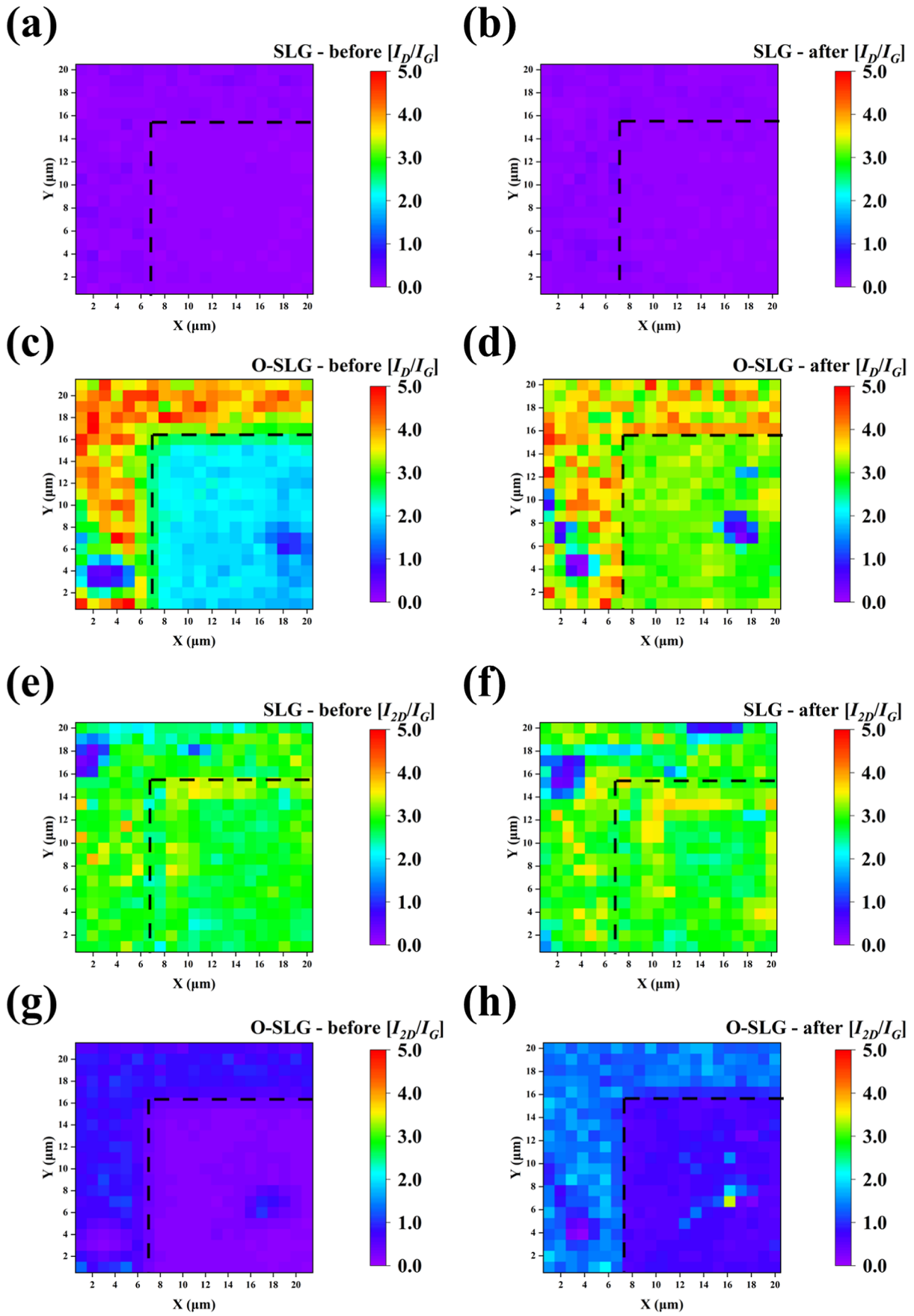


**Figure 2.** $I_D/I_G$ mapping of SLG (a) before and (b) after CV test. $I_D/I_G$ mapping of O-SLG (c) before and (d) after CV test. $I_{2D}/I_G$ mapping of SLG (e) before and (f) after CV. $I_{2D}/I_G$ mapping of O-SLG (g) before and (h) after CV test. The dashed line demarcates the boundary between areas with Au electrode underneath (upper left) and the bare SLG without Au (lower right).



https://doi.org/10.1021/acs.jpcc.5c02290
J. Phys. Chem. C 2025, 129, 14993−15002

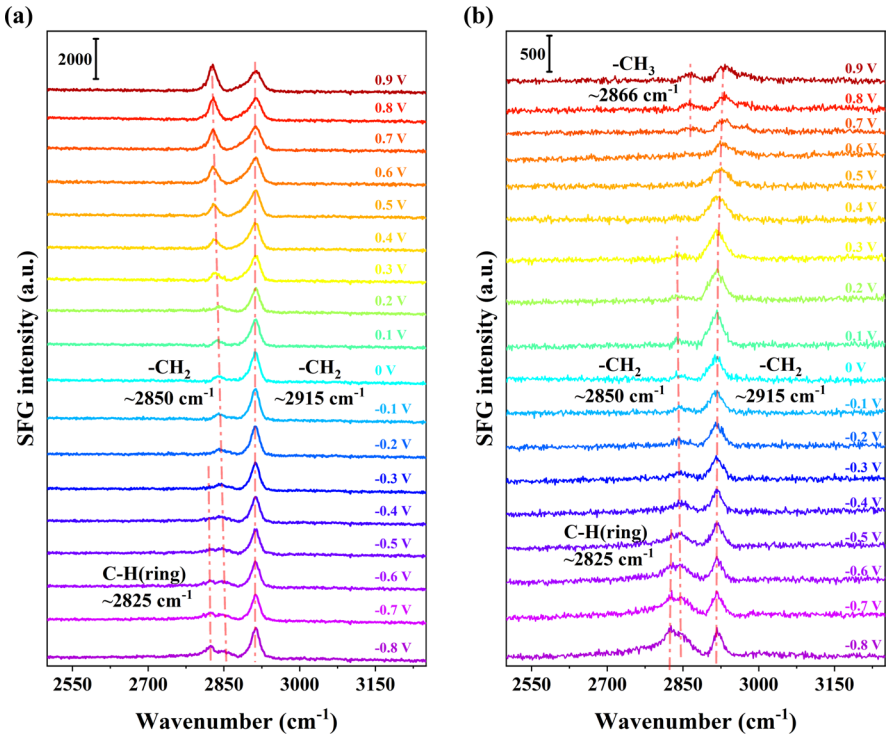


**Figure 3.** SFG spectra for $[EMIM]^+$ $[TFSI]^-$ on (a) SLG and (b) O-SLG at different voltages.

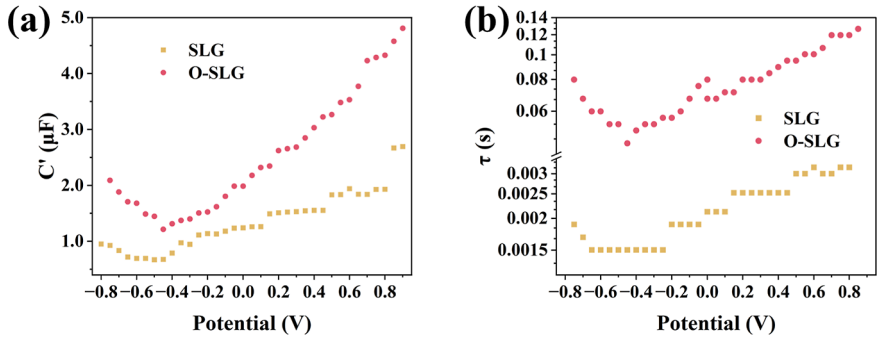


**Figure 4.** (a) Frequency-dependent capacitance ($C'$) and (b) relaxation time constant ($\tau_0$) of SLG and O-SLG as a function of voltage.

identical elemental composition between SLG and O-SLG (Figures S4 and S5) arises from substrate signal contributions, which dilute the surface-specific signatures. The increase in oxygenated species (C−O/C═O) shows the effect of surface functionalization, providing direct evidence of successful oxygen functionalization through plasma treatment.

AFM-IRFEL leverages the high spatial resolution of AFM and the tunable intense IRFEL, enabling nanoscale vibrational spectroscopy with unparalleled sensitivity to chemical modifications (Figure 1c). As shown in Figure 1d, the AFM imaging confirms that SLG maintains a highly flat surface morphology after oxygen functionalization, while the observed grooves may originate from the surface roughness of the quartz substrate. As an optically active nanomaterial, SLG can enhance vibrational spectroscopy signals through a chemical charge transfer mechanism,[32] amplifying the IR absorption of certain substrate modes. The corresponding IRFEL spectra reveal an IR peak at 812 cm$^{-1}$ in both samples, attributed to the Si−O−Si vibrational mode of the quartz substrate.[33] Notably, the reduced peak intensity in the O-SLG suggests that the oxygen functionalization disrupts the $\pi$-conjugation of graphene, thereby reducing the chemical enhancement effect. AFM topographical analysis reveals that oxygen plasma treatment induces measurable surface roughening and the root-mean-square roughness ($R_a$) increases from 0.729 nm (SLG) to 0.787 nm (O-SLG). On the other hand, since the functionalization would change the band structure and thus optical properties such as the refractive index ($n$) and extinction coefficient ($k$),[34] we have used ellipsometry, which characterizes the interaction between light and the electronic states by detecting wave polarization, to distinguish the change upon functionalization.[35] As shown in Figure 1e, $n$ and $k$ values of O-SLG lie between those of SLG and argon-treated SLG (Ar-SLG), suggesting that oxygen plasma treatment has caused changes in the electronic band structure of O-SLG by $\sigma$-states from C−O and $\pi$-states from C═O,[36] compared to SLG and Ar-SLG, aligning with the enhancement of $n$, $k$ for rGO compared to GO.[37] In addition, as a result of oxygen functionalization, the capacitance of O-SLG (14.88 $\mu$F cm$^{-2}$) is higher than that of the bare SLG (9.35 $\mu$F cm$^{-2}$), as estimated from the CV curves in Figure 1f, sharing with trends observed in carbon nanofibers[15] and activated carbon.[38] In


https://doi.org/10.1021/acs.jpcc.5c02290
J. Phys. Chem. C 2025, 129, 14993−15002

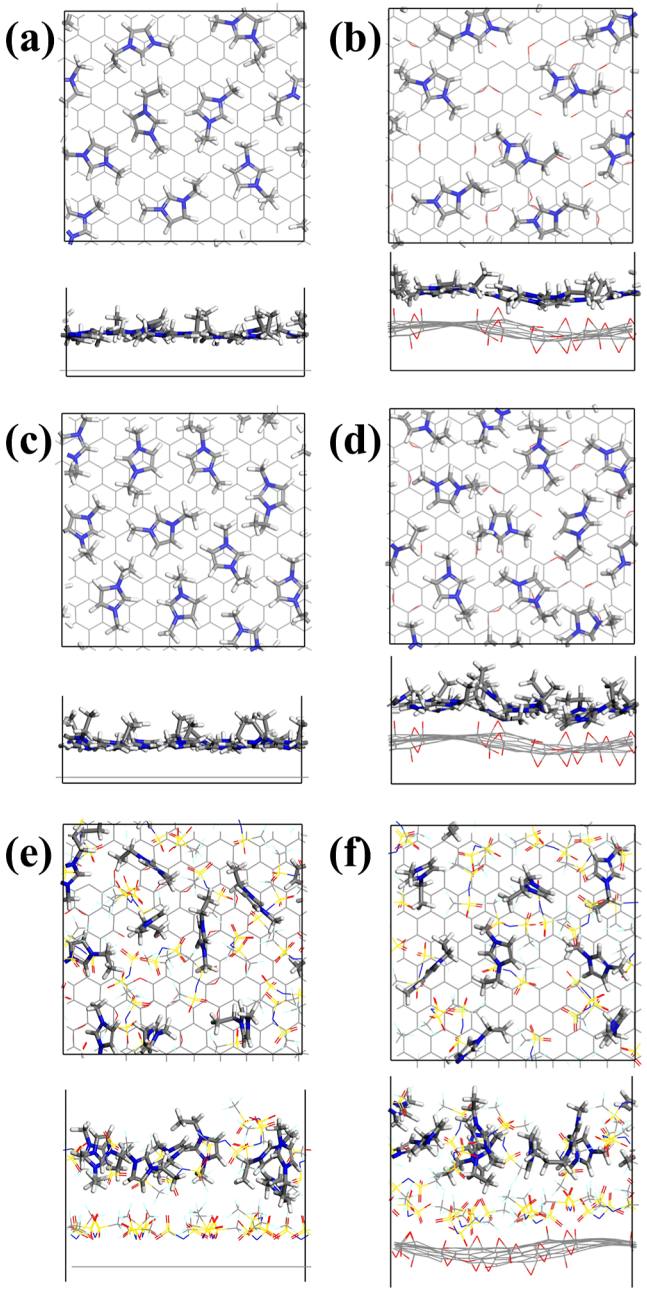


**Figure 5.** MD simulations of electrode interfaces at varying charge densities. (a) SLG, −0.03 e/C atom; (b) O-SLG, −0.03 e/C atom; (c) SLG, −0.06 e/C atom; (d) O-SLG, −0.06 e/C atom; (e) SLG, +0.06 e/C atom; (f) O-SLG, +0.06 e/C atom $[EMIM]^+$ cations (N atoms—blue, C backbone—gray, H atoms—white), $[TFSI]^-$ anions (S atoms—yellow, O atoms—red, F atoms-cyan, N atoms—blue).

comparison, the capacitance of SLG in 1-butyl-3-methylimidazolium hexafluorophosphate ($[BMIM]^+[PF_6]^-$) ionic liquid reported by Tao et al. is about 6 $\mu$F cm$^{-2}$,[39] indicating the validity of our protocol. To exclude the influence of substrates, comparative capacitance measurement was performed on sapphire and $CaF_2$. As shown in Figure S6, the spectral enhancement of O-SLG over SLG is consistent, confirming the substrate-independent nature of plasma-induced oxygen functionalization.

Previous study has shown that GO undergoes electrochemical reduction at a potential of −0.8 V in 0.1 M $Li^+[PF_6]^-$/AN.[16] To determine the influence of oxygen

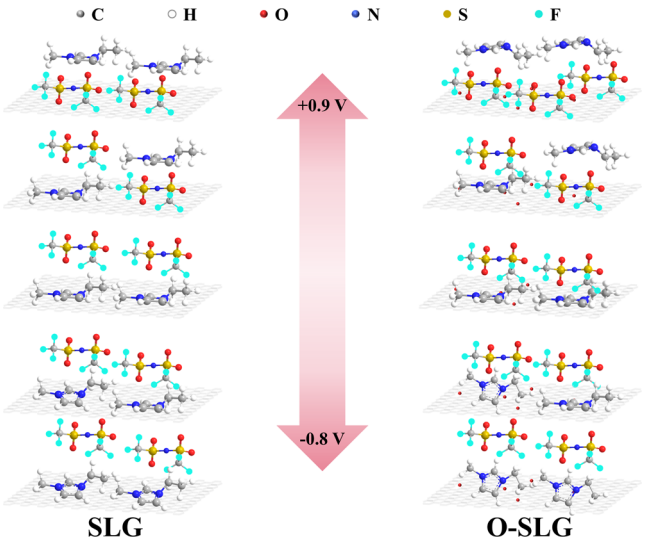


**Figure 6.** Schematic EDL structure of SLG and O-SLG at negative and positive potentials.

functional groups on the stability of O-SLG, CV was performed in an electrochemical window of −0.8 to +0.9 V (vs Pt), and the ex situ Raman mapping of the exactly same region was compared before and after CV for SLG or O-SLG. The evolution of defects has been quantified with $I_D/I_G$, where the D band (~1350 cm$^{-1}$) is associated with the number of defects in SLG.[40] In the measurement, a 10 $\mu$m-wide Au electrode was coated on the substrate before the transfer of SLG and the boundary (the dashed line in Figure 2) between SLG with Au underneath and the uncoated SLG has been used as a reference for position calibration. The SLG on Au exhibits a p-type doping due to the interfacial charge transfer.[41] Single-point Raman spectra (Figure S7) reveal substrate-sensitive features: pronounced peak shifts (>5 cm$^{-1}$) occur exclusively on Au, whereas quartz, $CaF_2$, and sapphire exhibit negligible displacement (<2 cm$^{-1}$). Despite this interfacial phenomenon, the critical stability metrics, i.e., $I_D/I_G$ > 2.0 for O-SLG and $I_{2D}/I_G$ > 2.0 for pristine SLG, remains consistent. In the mapping area of 20 × 20 $\mu$m$^2$, the Raman signal from the region of 12 × 12 $\mu$m$^2$ (lower right in Figure 2) exhibits a spectral signature dominated by SLG, which is the focus of analyses. From Figure 2a,b, the spatially averaged $I_D/I_G$ ratio of SLG in the demarcated region is ~0.052 (before CV) or ~0.049 (after CV), indicating the negligible change after CV and the great structural stability of SLG upon electrochemical cycling. In contrast, Figure 2c,d shows that O-SLG has a higher defect content after CV, as evidenced by the largely increased $I_D/I_G$ ratio from ~1.834 (before CV) to ~2.997 (after CV). The enhancement in $I_D/I_G$ ratio is similar to D-band amplification observed in rGO, suggesting oxygen-mediated defect generation after electrochemical polarization.[42]

The 2D band (~2700 cm$^{-1}$) in the Raman spectrum of graphene can also serve as a critical indicator of doping effects, where the intensity ratio of $I_{2D}/I_G$ increases for hole or electron doping.[43] Figure 2e,f shows the mapping evolution of the $I_{2D}/I_G$ ratio before and after CV for SLG. Again, we can see that the pristine SLG maintains an exceptional structural stability after cycling, evidenced by the very small variation (~2.77 before CV vs ~2.89 after CV). However, Figure 2g,h shows that O-SLG experiences a 203% enhancement in the $I_{2D}/I_G$ ratio (~0.243 before CV vs ~0.739 after CV), suggesting the


https://doi.org/10.1021/acs.jpcc.5c02290
J. Phys. Chem. C 2025, 129, 14993−15002

voltage-activated oxygen detachment as well. The observed increase in ratios of $I_D/I_G$ and $I_{2D}/I_G$ for O-SLG is attributed to the electrochemical reduction of oxygen-containing functional groups (mainly C−O and C═O moieties), which partially restores the conjugated networks but concurrently generates more topological defects, consistent with prior report.[16] Critically, the minimal Au coverage (0.06% of total area) ensures a negligible contribution to electrochemical property.

While Raman mapping unveils the structural evolution of the O-SLG, SFG spectroscopy directly correlates these morphological alterations with dynamic ion reconfiguration of the electric double layer (EDL), revealing how oxygen functionalization modulates the specific adsorption geometry of $[EMIM]^+$ cations. SFG measurement was conducted in a hermetically sealed cell containing a purified $[EMIM]^+[TFSI]^-$ electrolyte to minimize the interference of atmospheric water (Figure S1). The $[EMIM]^+[TFSI]^-$ ionic liquid was selected for the planar imidazolium ring that enables $\pi-\pi$ stacking on SLG,[44] forming a preadsorbed layer, with reorganization dynamics directly evidenced by potential-dependent SFG spectra (Figure 3). The interfacial architecture of the $[EMIM]^+$ cation is investigated through SFG spectroscopy (2300−3640 $cm^{-1}$), resolving three diagnostically critical modes: (i) the methylene symmetric stretching vibration ($-CH_{2,sym}$, ∼2850 $cm^{-1}$), (ii) the C−H vibration mode of the imidazolium ring (C−H, ∼2825 $cm^{-1}$), and (iii) the methylene Fermi resonance ($-CH_{2,FR}$, ∼2910 $cm^{-1}$), as systematically resolved in Figure 3.[22,45] The intensity of Fermi resonance peaks exhibits pronounced sensitivity to environmental coupling effects.[46] Therefore, the $-CH_{2,FR}$ peak is excluded from our spectral analysis to prevent misinterpretation arising from its pronounced sensitivity to environmental perturbations. The complete absence of methyl group vibrations ($N-CH_3$ and $C-CH_3$) for SLG at all potentials arises from orientation constraints: $N-CH_3$ adopts surface-parallel alignment in vertical ring configurations and becomes sterically shielded in planar states, whereas the dynamic disorder in the terminal methyl group cancels SFG-active dipole components. Note that the characteristic shift of the $-CH_{2,sym}$ during potential scan is conclusively attributed to the Stark effect arising from the interfacial electric field.[21] SFG spectral intensity heatmaps of $[EMIM]^+[TFSI]^-$ on SLG and O-SLG under applied potentials are shown in Figure S8.

Figure 3a shows the voltage-dependent SFG spectra of SLG, revealing potential-driven interfacial restructuring of $[EMIM]^+$ cations on SLG. The interfacial molecular reconfiguration of $[EMIM]^+$ cations under voltage modulation is revealed through PPP-polarized SFG spectroscopy: at negative potentials (−0.3 to −0.8 V), electrostatic attraction drives the imidazolium ring from a surface-parallel to near-vertical orientation, amplifying the vertical dipole component of aromatic C−H vibrations and inducing a 500 a.u. intensity surge at −0.8 V. Notably, the $-CH_{2,sym}$ (∼2850 $cm^{-1}$) exhibits a relatively stable signal intensity across this range, consistent with in situ electrochemical quartz crystal microbalance (EQCM) data that the process involves cationic interfacial rearrangement rather than a net increase in adsorption density.[47] This indicates that the tilting of the imidazolium ring does not significantly alter the surface coverage of cations. Conversely, positive polarization drives interfacial depletion of cations through electrostatic repulsion, suppressing C−H vibrations while enhancing ethyl chain−surface interactions: the progressive $-CH_{2,sym}$ signal intensification with positive potential suggests hydrophobic-driven configurational reorganization of the alkyl chains, characterized by upright $-CH_2$ aligned perpendicular to the surface.

A very different behavior emerges on the O-SLG. Figure 3b shows distinct signal changes: on the surface of the O-SLG (Figure 3b), oxygen-containing functional groups reconfigure interfacial dynamics through chemical bonding−electrostatic synergistic interactions. Under negative polarization (0 to −0.8 V), oxygen-containing functional groups anchor the imidazolium ring in a near-planar orientation, while the strong electrostatic field induces a tilt of the ring, causing the C−H peak (∼2825 $cm^{-1}$) to emerge at −0.5 V and intensify to 430 a.u. at −0.8 V. Concurrently, the $-CH_{2,sym}$ signal intensity surges from 84 a.u. at 0 V to 347 a.u. at −0.8 V (an increase of 313%), likely accompanied by localized cationic enrichment at the interface. At positive potentials, electrostatic cation repulsion dominates over hydrophobic effects, causing ethyl detachment: evidenced by signal attenuation to <70 a.u. at +0.9 V. At ≥0.7 V, a distinct peak at 2866 $cm^{-1}$ emerges. This signature corresponds to a $-CH_3$ symmetric stretch, although electrostatic field and oxygenated functional groups force methyl groups to tilt from surface parallel confinement.

Based on SFG-identified correlations between oxygen functionalization and cation adsorption reconfiguration, we employed EIS to elucidate how these structural modifications govern the interfacial ionic relaxation dynamics and charge storage capacity of the O-SLG. Impedance spectra were collected at various voltages (−0.8 to +0.9 V, 0.05 V/step). The imaginary part of the capacitance ($C''$) exhibits a characteristic maximum at a characteristic frequency $f_0$ as shown in Figure S9, which defines the fundamental relaxation time constant ($\tau_0$) as $\tau_0 = 1/(2\pi f_0)$, and $\tau_0$ physically corresponds to the RC time constant ($\tau_0 = R_sC$, where $R_s$ denotes the equivalent series resistance and $C$ the capacitance).[48] Smaller $\tau_0$ values indicate an optimized ion transport efficiency across the electrode−electrolyte interface.[48] Through analysis of impedance data, the real part of the capacitance ($C'$) at the $\tau_0$ was found to reach half of the low-frequency limit capacitance ($C_{LF}$).[49] $C_{LF}$ is proportionate to the EDL capacitance ($C_{dl}$),[48] and $C_{dl}$ is proportionate to $2C'$. As shown in Figure 4a, the potential-dependent capacitance profiles indicate that the O-SLG exhibits an enhancement of more than 135% in double-layer capacitance compared to SLG across the applied potential range (−0.8 to +0.9 V); the enhanced capacitance of the O-SLG arises from oxygen moieties (e.g., C−O/C═O) synergistic coupling as shown in the SFG spectrum. A negative shift in the point of zero charge (PZC) from −0.2 V for pristine SLG to −0.5 V for O-SLG correlates with the oxygen functionalization. By changing the configuration of absorbed ions, as described above, the charge-transfer relaxation time for SLG ($\tau_0$ = 2.3 ms at +0.3 V) is ∼34-fold shorter than that for O-SLG ($\tau_0$ = 78 ms), showing that O-SLG has a much slower migration or response of ions, as shown in Figure 4b. In the cathodic regime (−0.6 to −0.2 V), $\tau_0$ stability reflects a static cation compact layer ($[EMIM]^+$) with invariant interfacial capacitance, mechanistically linked to ion mass conservation on SLG under negative polarization as quantified by in situ EQCM.[47] Notably, at extreme cathodic potentials (−0.8 to −0.7 V), a secondary $\tau_0$ rise emerges, likely attributable to cation migration toward the electrode surface driven by concentration polarization. In contrast, the O-SLG displays progressive $\tau_0$ changes below the PZC and may originate from migration-dominated EDL


https://doi.org/10.1021/acs.jpcc.5c02290
J. Phys. Chem. C 2025, 129, 14993−15002

reorganization. This observation suggests that while the presence of oxygen functional groups enhance the capacitance of the SLG electrode, ionic kinetics of the EDL has been deteriorated.

To elucidate the atomic origins of the potential-dependent capacitance enhancement and interfacial ion reorganization observed, we performed MD simulations to probe the EDL restructuring on the SLG and the O-SLG electrodes. Figure 5a–d shows that, at fixed negative charge density (e.g., −0.06 e/C atom), both SLG and the O-SLG exhibit $[EMIM]^+$ ring tilting compared to the situation of lower charge density (−0.03 e/C atom), consistent with potential-driven vertical reorientation from SFG (Figure 3). Critically, at −0.06 e/C atom, O-SLG induces a significantly larger tilt angle, revealing that oxygen groups anchor the ring near-parallel at low electric fields but amplify electrostatic-driven tilting under high charge density. This synergism also explains the SFG observations of C−H ring vibration emergence at −0.5 V and 313% $-CH_{2,sym}$ intensity surge on the O-SLG (vs stable signal on the SLG), indicating the cationic enrichment via functionalization-enhanced adsorption. Notably, the more negative PZC of O-SLG (−0.5 V vs −0.2 V for SLG) implies that identical charge density corresponds to a less negative absolute potential on O-SLG. Despite this, O-SLG exhibits a stronger response, underscoring the dominant role of chemical modification over electrostatic potential shift. As shown in Figure 5e,f, $[EMIM]^+$ in the secondary layer on the O-SLG adopts a more vertical alkyl chain orientation and resides closer to the electrode for a bias of +0.06 e/C atom. This computational finding complements SFG data: while SFG detects an interfacial cation depletion (attenuated $-CH_{2,sym}$ signal), the restructured secondary layer may contribute to the emergent $-CH_3$ peak at 2866 $cm^{-1}$ (Figure 3b), attributed to the $-CH_3$ tilt forced by oxygen-induced confinement. As shown in Figure S10, DFT calculations reveal that when a single $[EMIM]^+$ ion adsorbs on SLG and O-SLG, the methyl group of $[EMIM]^+$ is positioned in closer proximity to O-SLG compared to SLG. Figure 6 schematically contrasts the potential-dependent adsorption configurations for SLG and O-SLG, where the compact secondary layer on the O-SLG enhances the charge storage capacity, but its rigidity may hinder the ion relaxation kinetics, well aligning with the slower dynamics of EIS for the O-SLG.

## CONCLUSIONS

In summary, we have provided insights into the role of oxygen functionalization in electrochemical stability and interfacial charge storage of graphene-based supercapacitor electrodes. The intensity mapping of Raman spectra shows the reduced oxygen functionalization and increased defect density in O-SLG after cycling, in contrast to the pristine SLG. This structural evolution is caused by interfacial ion organization, as in situ SFG spectroscopy reveals that the $[EMIM]^+$ cations adopt a near-planar orientation through anchoring at oxygenated sites under negative potential (0 to −0.8 V), followed by enhanced net charge density of anions under positive potential (0 to ∼0.9 V). This is different from the situation on pristine SLG, where the $[EMIM]^+$ adopts a tilted adsorption geometry under a negative potential, whereas a positive potential triggers ring depletion alongside alkyl-chain anchoring. These interfacial differences directly impact ionic dynamics, with EIS comparison demonstrating that oxygen functionalization has caused slower ionic relaxation while providing more storage capacity. By MD and DFT, we confirm that oxygen groups on SLG anchor ions more strongly, increasing the capacitance by packing ions near the surface. These findings highlight the importance of optimizing the content and type of functional groups to balance capacity improvement with material stability and ionic kinetics.

## ASSOCIATED CONTENT

### Data Availability Statement

All data needed to evaluate the conclusions in the paper are present in the paper and/or the Supporting Information. Additional data related to this paper may be requested from the authors.

### Supporting Information

The Supporting Information is available free of charge at https://pubs.acs.org/doi/10.1021/acs.jpcc.5c02290.

Schematic diagram of an in situ electrochemical device, MD simulation models, SEM and EDS of SLG on quartz, SFG spectral intensity heatmaps, frequency-dependent $C''$ vs $C'$ profiles for SLG and O-SLG electrodes at −0.3 V, and DFT simulation of $[EMIM]^+$ on SLG and O-SLG (PDF)

## AUTHOR INFORMATION


### Corresponding Authors

**Jiawei Xue** − *National Synchrotron Radiation Laboratory, University of Science and Technology of China, Hefei, Anhui 230029, China;* orcid.org/0000-0003-3693-4115; Email: xuejw@ustc.edu.cn

**Yanwu Zhu** − *Department of Materials Science and Engineering, School of Chemistry and Materials Science, University of Science and Technology of China, Hefei, Anhui 230026, China; State Key Laboratory of Precision and Intelligent Chemistry and Hefei National Research Center for Physical Sciences at the Microscale, University of Science and Technology of China, Hefei, Anhui 230026, China;* orcid.org/0000-0002-7505-1502; Email: zhuyanwu@ustc.edu.cn

### Authors

**Xiaolan Wang** − *Department of Materials Science and Engineering, School of Chemistry and Materials Science, University of Science and Technology of China, Hefei, Anhui 230026, China*

**Wei Guo** − *National Synchrotron Radiation Laboratory, University of Science and Technology of China, Hefei, Anhui 230029, China;* orcid.org/0000-0003-1274-2979

**Kun Ni** − *Department of Materials Science and Engineering, School of Chemistry and Materials Science, University of Science and Technology of China, Hefei, Anhui 230026, China*

**Jun Ma** − *The USTC Center for Micro and Nanoscale Research and Fabrication, University of Science and Technology of China, Hefei, Anhui 230026, China*

**Zhaohui Wang** − *State Key Laboratory of Physical Chemistry of Solid Surfaces, MOE Key Laboratory of Spectrochemical Analysis and Instrumentation, Department of Chemistry, College of Chemistry and Chemical Engineering, Xiamen University, Xiamen, Fujian 361005, China;* orcid.org/0000-0003-3847-8037

**Jun Bao** − *National Synchrotron Radiation Laboratory and Collaborative Innovation Center of Chemistry for Energy*




https://doi.org/10.1021/acs.jpcc.5c02290
J. Phys. Chem. C 2025, 129, 14993−15002

*Materials (iChEM), University of Science and Technology of China, Hefei, Anhui 230029, China; State Key Laboratory of Precision and Intelligent Chemistry, University of Science and Technology of China, Hefei, Anhui 230026, China;*
orcid.org/0000-0002-1812-8999

Complete contact information is available at:
https://pubs.acs.org/10.1021/acs.jpcc.5c02290

### Author Contributions

[▽]X.W., W.G., and K.N. contributed equally to this work. X.W. performed most experiments, data analysis, and manuscript writing. W.G. helped to perform the characterization of SFG and data analysis. K.N. performed the simulations and revised the manuscript. J.M. helped to perform the characterization of ellipsometry. J.X. helped in data analysis, supervised the IRFEL experiment, and revised the manuscript. Z.W. discussed the experimental results. J.B gave the support on the SFG. Y.Z. supervised the study, manuscript drafting, and final approval.

### Notes

The authors declare no competing financial interest.

## ■ ACKNOWLEDGMENTS

This work was supported by the National Natural Science Foundation of China (Nos. 52273239, 52325202, 12241502, and 22202188), the National Key Research and Development Program of China (No. 2021YFA1600800), the China Postdoctoral Science Foundation (No. 2024T170885), the Fundamental Research Funds for the Central Universities (Nos. WK2310000116, WK2310000124, and 20720220010), the USTC Synchrotron Radiation Joint Fund (No. KY9990000203), and the Xiaomi Young Scholars. The USTC Center for Micro and Nanoscale Research and Fabrication and the AFM-IRFEL and IRFEL-SFG stations of FELiChEM free electron laser facility (supported by the National Science Foundation of China under contract No. 21327901), National Synchrotron Radiation Laboratory, Hefei, China, are appreciated.

## ■ REFERENCES

(1) Liu, X.; Lyu, D.; Merlet, C.; Leesmith, M. J. A.; Hua, X.; Xu, Z.; Grey, C. P.; Forse, A. C. Structural disorder determines capacitance in nanoporous carbons. *Science* **2024**, *384* (6693), 321−325.
(2) Qing, Y.; Jiang, Y.; Lin, H.; Wang, L.; Liu, A.; Cao, Y.; Sheng, R.; Guo, Y.; Fan, C.; Zhang, S.; et al. Boosting the supercapacitor performance of activated carbon by constructing overall conductive networks using graphene quantum dots. *J. Mater. Chem. A* **2019**, *7* (11), 6021−6027.
(3) Li, Z. J.; Yang, B. C.; Zhang, S. R.; Zhao, C. M. Graphene oxide with improved electrical conductivity for supercapacitor electrodes. *Appl. Surf. Sci.* **2012**, *258* (8), 3726−3731.
(4) Zhang, S.; Wang, H.; Liu, J.; Bao, C. Measuring the specific surface area of monolayer graphene oxide in water. *Mater. Lett.* **2020**, *261*, 127098.
(5) Zhu, Y.; Murali, S.; Stoller, M. D.; Ganesh, K. J.; Cai, W.; Ferreira, P. J.; Pirkle, A.; Wallace, R. M.; Cychosz, K. A.; Thommes, M.; et al. Carbon-Based Supercapacitors Produced by Activation of Graphene. *Science* **2011**, *332* (6037), 1537−1541.
(6) Yang, X.; Cheng, C.; Wang, Y.; Qiu, L.; Li, D. Liquid-Mediated Dense Integration of Graphene Materials for Compact Capacitive Energy Storage. *Science* **2013**, *341* (6145), 534−537.
(7) Li, Z.; Gadipelli, S.; Li, H.; Howard, C. A.; Brett, D. J. L.; Shearing, P. R.; Guo, Z.; Parkin, I. P.; Li, F. Tuning the interlayer spacing of graphene laminate films for efficient pore utilization towards compact capacitive energy storage. *Nat. Energy* **2020**, *5* (2), 160−168.
(8) Zhao, Y.; Hu, C.; Hu, Y.; Cheng, H.; Shi, G.; Qu, L. A Versatile, Ultralight, Nitrogen-Doped Graphene Framework. *Angew. Chem., Int. Ed.* **2012**, *51* (45), 11371−11375.
(9) Wu, Z.-S.; Tan, Y.-Z.; Zheng, S.; Wang, S.; Parvez, K.; Qin, J.; Shi, X.; Sun, C.; Bao, X.; Feng, X.; et al. Bottom-Up Fabrication of Sulfur-Doped Graphene Films Derived from Sulfur-Annulated Nanographene for Ultrahigh Volumetric Capacitance Micro-Supercapacitors. *J. Am. Chem. Soc.* **2017**, *139* (12), 4506−4512.
(10) Kim, J.; Wi, S. M.; Son, S.; Lim, H.; Park, Y.; Jang, A. R.; Park, J. B.; Cho, Y.; Song, Y.-C.; Pak, S.; et al. Rationally engineered interdigitated electrodes with heteroatom doped porous graphene and improved surface wettability for flexible micro-supercapacitors. *J. Energy Storage* **2024**, *86*, 111271.
(11) Iamprasertkun, P.; Krittayavathananon, A.; Seubsai, A.; Chanlek, N.; Kidkhunthod, P.; Sangthong, W.; Maensiri, S.; Yimnirun, R.; Nilmoung, S.; Pannopard, P.; et al. Charge storage mechanisms of manganese oxide nanosheets and N-doped reduced graphene oxide aerogel for high-performance asymmetric supercapacitors. *Sci. Rep.* **2016**, *6* (1), 37560.
(12) Hou, J.; Cao, C.; Idrees, F.; Ma, X. Hierarchical Porous Nitrogen-Doped Carbon Nanosheets Derived from Silk for Ultrahigh-Capacity Battery Anodes and Supercapacitors. *ACS Nano* **2015**, *9* (3), 2556−2564.
(13) Chen, J.; Han, Y.; Kong, X.; Deng, X.; Park, H. J.; Guo, Y.; Jin, S.; Qi, Z.; Lee, Z.; Qiao, Z.; et al. The Origin of Improved Electrical Double-Layer Capacitance by Inclusion of Topological Defects and Dopants in Graphene for Supercapacitors. *Angew. Chem., Int. Ed.* **2016**, *55* (44), 13822−13827.
(14) Chen, Y.; Zhang, Z.; Huang, Z.; Zhang, H. Effects of oxygen-containing functional groups on the supercapacitor performance of incompletely reduced graphene oxides. *Int. J. Hydrogen Energy* **2017**, *42* (10), 7186−7194.
(15) He, Y.; Zhang, Y.; Li, X.; Lv, Z.; Wang, X.; Liu, Z.; Huang, X. Capacitive mechanism of oxygen functional groups on carbon surface in supercapacitors. *Electrochim. Acta* **2018**, *282*, 618−625.
(16) Viinikanoja, A.; Kauppila, J.; Damlin, P.; Suominen, M.; Kvarnström, C. In situ FTIR and Raman spectroelectrochemical characterization of graphene oxide upon electrochemical reduction in organic solvents. *Phys. Chem. Chem. Phys.* **2015**, *17* (18), 12115−12123.
(17) Liu, Q.; Xu, H.; Ma, C.; Qiao, W.; Ling, L.; Zhang, Y.; Zhang, X.; Wang, J. Boosting anions storage via union of in-situ N doping and mesoporous hollow hard carbon nanospheres for advanced dual-ion capacitors. *Chem. Eng. Sci.* **2024**, *298*, 120354.
(18) Wang, W.-W.; Yan, H.; Gu, Y.; Yan, J.; Mao, B.-W. In Situ Electrochemical Atomic Force Microscopy: From Interfaces to Interphases. *Annu. Rev. Anal. Chem.* **2024**, *17* (17), 103−126.
(19) Hatakeyama, Y.; Futamura, R. Advances in Electric Double-Layer Capacitor Research Using X-ray Scattering Techniques. *Electrochemistry* **2024**, *92* (7), 074004.
(20) Zaera, F. Probing Liquid/Solid Interfaces at the Molecular Level. *Chem. Rev.* **2012**, *112* (5), 2920−2986.
(21) Baldelli, S. Probing Electric Fields at the Ionic Liquid−Electrode Interface Using Sum Frequency Generation Spectroscopy and Electrochemistry. *J. Phys. Chem. B* **2005**, *109* (27), 13049−13051.
(22) Baldelli, S.; Bao, J.; Wu, W.; Pei, S.-s. Sum frequency generation study on the orientation of room-temperature ionic liquid at the graphene−ionic liquid interface. *Chem. Phys. Lett.* **2011**, *516* (4), 171−173.
(23) Baldelli, S. Interfacial Structure of Room-Temperature Ionic Liquids at the Solid−Liquid Interface as Probed by Sum Frequency Generation Spectroscopy. *J. Phys. Chem. Lett.* **2013**, *4* (2), 244−252.
(24) Xu, S.; Xing, S.; Pei, S.-S.; Ivaništšev, V.; Lynden-Bell, R.; Baldelli, S. Molecular Response of 1-Butyl-3-Methylimidazolium Dicyanamide Ionic Liquid at the Graphene Electrode Interface Investigated by Sum Frequency Generation Spectroscopy and

Molecular Dynamics Simulations. *J. Phys. Chem. C* **2015**, *119* (46), 26009−26019.
(25) Li, H.; Singh, A.; Bayram, F.; Childress, A. S.; Rao, A. M.; Koley, G. Impact of oxygen plasma treatment on carrier transport and molecular adsorption in graphene. *Nanoscale* **2019**, *11* (23), 11145−11151.
(26) Hafner, J. Ab-initio simulations of materials using VASP: Density-functional theory and beyond. *J. Comput. Chem.* **2008**, *29* (13), 2044−2078.
(27) Ernzerhof, M.; Scuseria, G. E. Assessment of the Perdew−Burke−Ernzerhof exchange-correlation functional. *J. Chem. Phys.* **1999**, *110* (11), 5029−5036.
(28) Perdew, J. P.; Burke, K.; Ernzerhof, M. Generalized Gradient Approximation Made Simple. *Phys. Rev. Lett.* **1996**, *77* (18), 3865−3868.
(29) Grimme, S.; Antony, J.; Ehrlich, S.; Krieg, H. A consistent and accurate ab initio parametrization of density functional dispersion correction (DFT-D) for the 94 elements H-Pu. *J. Chem. Phys.* **2010**, *132* (15), 154104.
(30) Grimme, S.; Antony, J.; Ehrlich, S.; Krieg, H. A consistent and accurate ab initio parametrization of density functional dispersion correction (DFT-D) for the 94 elements H-Pu. *J. Chem. Phys.* **2010**, *132* (15), 154104.
(31) Parry, K. L.; Shard, A. G.; Short, R. D.; White, R. G.; Whittle, J. D.; Wright, A. ARXPS characterisation of plasma polymerised surface chemical gradients. *Surf. Interface Anal.* **2006**, *38* (11), 1497−1504.
(32) Ling, X.; Xie, L.; Fang, Y.; Xu, H.; Zhang, H.; Kong, J.; Dresselhaus, M. S.; Zhang, J.; Liu, Z. Can Graphene be used as a Substrate for Raman Enhancement? *Nano Lett.* **2010**, *10* (2), 553−561.
(33) Liu, H.; Kaya, H.; Lin, Y.-T.; Ogrinc, A.; Kim, S. H. Vibrational spectroscopy analysis of silica and silicate glass networks. *J. Am. Ceram. Soc.* **2022**, *105* (4), 2355−2384.
(34) Yoo, S.; Park, Q.-H. Spectroscopic ellipsometry for low-dimensional materials and heterostructures. *Nanophotonics* **2022**, *11* (12), 2811−2825.
(35) Humlíček, J. Polarized Light and Ellipsometry. In *Handbook of Ellipsometry*; Tompkins, H. G., Irene, E. A., Eds.; Springer Berlin Heidelberg, 2005; pp 3−91.
(36) Losurdo, M.; Giangregorio, M. M.; Bianco, G. V.; Capezzuto, P.; Bruno, G. How spectroscopic ellipsometry can aid graphene technology? *Thin Solid Films* **2014**, *571*, 389−394.
(37) Jung, I.; Vaupel, M.; Pelton, M.; Piner, R.; Dikin, D. A.; Stankovich, S.; An, J.; Ruoff, R. S. Characterization of Thermally Reduced Graphene Oxide by Imaging Ellipsometry. *J. Phys. Chem. C* **2008**, *112* (23), 8499−8506.
(38) Yuan, S.; Huang, X.; Wang, H.; Xie, L.; Cheng, J.; Kong, Q.; Sun, G.; Chen, C.-M. Structure evolution of oxygen removal from porous carbon for optimizing supercapacitor performance. *J. Energy Chem.* **2020**, *51*, 396−404.
(39) Xia, J.; Chen, F.; Li, J.; Tao, N. Measurement of the quantum capacitance of graphene. *Nat. Nanotechnol.* **2009**, *4* (8), 505−509.
(40) Compagnini, G.; Giannazzo, F.; Sonde, S.; Raineri, V.; Rimini, E. Ion irradiation and defect formation in single layer graphene. *Carbon* **2009**, *47* (14), 3201−3207.
(41) Vanin, M.; Mortensen, J. J.; Kelkkanen, A. K.; Garcia-Lastra, J. M.; Thygesen, K. S.; Jacobsen, K. W. Graphene on metals: A van der Waals density functional study. *Phys. Rev. B* **2010**, *81* (8), 081408.
(42) Lee, A. Y.; Yang, K.; Anh, N. D.; Park, C.; Lee, S. M.; Lee, T. G.; Jeong, M. S. Raman study of D* band in graphene oxide and its correlation with reduction. *Appl. Surf. Sci.* **2021**, *536*, 147990.
(43) Das, A.; Pisana, S.; Chakraborty, B.; Piscanec, S.; Saha, S. K.; Waghmare, U. V.; Novoselov, K. S.; Krishnamurthy, H. R.; Geim, A. K.; Ferrari, A. C.; et al. Monitoring dopants by Raman scattering in an electrochemically top-gated graphene transistor. *Nat. Nanotechnol.* **2008**, *3* (4), 210−215.
(44) Paek, E.; Pak, A. J.; Hwang, G. S. A Computational Study of the Interfacial Structure and Capacitance of Graphene in [BMIM][PF6] Ionic Liquid. *J. Electrochem. Soc.* **2013**, *160* (1), A1.
(45) Rivera-Rubero, S.; Baldelli, S. Surface Characterization of 1-Butyl-3-methylimidazolium Br-, I-, PF6-, BF4-, (CF3SO2)2N-, SCN-, CH3SO3-, CH3SO4-, and (CN)2N- Ionic Liquids by Sum Frequency Generation. *J. Phys. Chem. B* **2006**, *110* (10), 4756−4765.
(46) Kish, E.; Mendes Pinto, M. M.; Bovi, D.; Basire, M.; Guidoni, L.; Vuilleumier, R.; Robert, B.; Spezia, R.; Mezzetti, A. Fermi Resonance as a Tool for Probing Peridinin Environment. *J. Phys. Chem. B* **2014**, *118* (22), 5873−5881.
(47) Ye, J.; Wu, Y.-C.; Xu, K.; Ni, K.; Shu, N.; Taberna, P.-L.; Zhu, Y.; Simon, P. Charge Storage Mechanisms of Single-Layer Graphene in Ionic Liquid. *J. Am. Chem. Soc.* **2019**, *141* (42), 16559−16563.
(48) Itagaki, M.; Suzuki, S.; Shitanda, I.; Watanabe, K. Electrochemical Impedance and Complex Capacitance to Interpret Electrochemical Capacitor. *Electrochemistry* **2007**, *75* (8), 649−655.
(49) Taberna, P. L.; Simon, P.; Fauvarque, J. F. Electrochemical Characteristics and Impedance Spectroscopy Studies of Carbon-Carbon Supercapacitors. *J. Electrochem. Soc.* **2003**, *150* (3), A292.




https://doi.org/10.1021/acs.jpcc.5c02290
J. Phys. Chem. C 2025, 129, 14993−15002